Catalysis Science & Technology

ROYAL SOCIETY OF CHEMISTRY

PAPER

View Article Online
View Journal | View Issue

Cite this: *Catal. Sci. Technol.*, 2025, 15, 4838

Cobalt-doped MIL-88A anchored on a cellulose filter paper: a recyclable flow-through catalyst for peroxymonosulfate activation during the degradation of organic dyes†

Yaru Li,‡[a] Jing-jing Shao,‡[a] Thomas L. Eberhardt[b] and Hui Pan *[a]

Received 3rd April 2025,
Accepted 28th June 2025

DOI: 10.1039/d5cy00412h

rsc.li/catalysis

To demonstrate the effective use of a heterogeneous catalyst for the treatment of wastewater in a flowing state, we synthesized a metal–organic framework, MIL-88A, *in situ* on a filter paper. A cobalt doping modification yielded a composite catalyst, Co-doped MIL-88A, on a filter paper (Co-M88A-FP), which was then used to activate peroxymonosulfate (PMS). Characterizations of Co-M88A-FP catalyst revealed that the morphology and structure of MIL-88A did not change when synthesized on the filter paper; however, the surface of MIL-88A became rough and amorphous after Co doping. The Co-M88A-FP/PMS catalytic system exhibited highly efficient degradation of rhodamine B (a test pollutant dye) and appeared to be adaptable to continuous flow conditions. XPS, EPR and radical scavenging test results indicated that singlet oxygen was the reactive species that mainly contributed to the degradation of the test pollutant dye. Therefore, it was revealed that electron-rich substances with low steric hindrance would be degraded more quickly by the Co-M88A-FP/PMS system.

1. Introduction

In recent years, there has been an increasing concern regarding the removal/treatment of dyes in wastewater.[1,2] Dyes have the potential to cause severe water contamination, resulting in various health issues owing to their toxic, carcinogenic, allergic, and mutagenic effects.[3,4] Hence, it is imperative to find effective treatment technologies to manage the environmental release of dyes from wastewaters. Rhodamine B (RhB), a common synthetic xanthene dye, is widely used as a colorant and tracer fluorescent agent and gets released in large quantities into the environment.[5] Traditional wastewater treatment technologies, such as activated sludge processes, have proven to be ineffective in digesting synthetic dyes as such because of their high chemical stability.[6] Accordingly, there remains a need to develop more effective dye removal methods from wastewaters.

Among the various treatment approaches, sulfate-radical-based advanced oxidation processes (SR-AOPs) have gained significant attention owing to their high oxidation potential and adaptability across a wide pH range. SR-AOPs using various reactive oxygen species (ROS), including sulfate radicals ($SO_4^{\bullet-}$), hydroxyl radicals ($^{\bullet}OH$), superoxide anions ($O_2^{\bullet-}$), and singlet oxygen ($^1O_2$), are recognized as attractive methods for wastewater treatment to degrade various pollutants.[7] Unlike the conventional Fenton reaction, in which H_2O_2 is commonly used as the oxidant, SR-AOPs use peroxymonosulfate (PMS) as the oxidant. The wide working pH range and easy transportation of PMS broaden its universal application.[8,9] Based on previous studies, transition metals (Co^{2+}, Fe^{2+}, and Mn^{2+}) have been shown to be promising candidates for effective PMS activation;[10–12] however, the use of these metal ions with heterogeneous catalytic systems is hampered by their high solubility, poor stability, and high toxicity, causing secondary contamination. Therefore, it is essential to explore heterogeneous catalysts with low metal ion leaching, high stability, and high activity.

Metal–organic frameworks (MOFs) are three-dimensional frameworks formed by metal centers and organic ligands; they have ultra-high surface areas and rich active sites and are structurally customizable. As a class of porous materials, they display superior potential for applications in drug delivery, gas and liquid separation, sensing, absorption, and catalysis. In particular, MOFs have been used to develop SR-AOPs for wastewater treatment.[13,14] MIL-88A (Fe) is one of the classic MOFs that is prepared from fumarate and Fe^{3+} ions, making it less toxic, cost-effective, and easy to synthesize.[15] Recently,

[a] *Jiangsu CoInnovation Center for Efficient Processing and Utilization of Forest Resources, Nanjing Forestry University, 159 Longpan Road, 210037, Nanjing, PR China. E-mail: Hpan@njfu.edu.cn*
[b] *USDA Forest Service, Forest Products Laboratory, One Gifford Pinchot Drive, Madison, WI 53726, USA*

† Electronic supplementary information (ESI) available. See DOI: https://doi.org/10.1039/d5cy00412h

‡ Yaru Li and Jing-jing Shao contributed equally to this work.

MIL-88A has been studied for the development of SR-AOPs for activating PMS. Zhang *et al.* used MIL-88A as a SR-AOP catalyst for tetracycline hydrochloride degradation, which, when combined with photocatalysis, provided a system to efficiently degrade this antibiotic.[16]

Alternatively, considering the synergistic contribution of different metals to PMS activation, bimetallic-MOF-based catalysts are gaining wide attention.[17–20] Cobalt is recognized as a very effective and ubiquitous metal for PMS activation, which can substantially enhance the catalytic activity.[21,22] Moreover, the leaching of Co ions can be significantly reduced owing to their coordination interactions with other metals. Luong *et al.* synthesized a CuCo–zeolitic imidazolate framework catalyst as a novel Fenton-like catalyst for the degradation of methyl orange and methylene blue.[23] However, the direct use of MOFs still faces some limitations. Specifically, catalyst powders are difficult to separate and recover during batchwise wastewater treatment processes, and they, in themselves, are not amenable to wastewater treatment systems that rely on continuous flow conditions. Monometallic active center stability and flexible framework dynamic adaptability significantly outperform the uncontrollable synergistic effects of the bimetallic system and the mass transfer limitations of the powdered MOF.

To overcome these problems, anchoring the MOF on a proper carrier is a feasible approach. Renewable cellulose fibers from biomass can serve as a low-cost, high-surface-area substrate and, in the form of filter paper (FP), provide a potential carrier for loading powder catalysts, affording advantages of low cost, a high number of active sites, and environmental friendliness. These unique advantages are attributed to the following two points: (i) a high porosity that makes circulation possible and (ii) environmentally friendly recyclability compared to that of synthetic carriers. In a study by Yang *et al.*, FP was used to load chitosan-templated MnO_2 nanoparticles, and the resultant catalyst system was used to remove methylene blue *via* Fenton-like degradation.[24] In this study, MIL-88A (M88A) was immobilized on FP by synthesizing it *in situ* and then doping it with cobalt to obtain a Co-doped MIL-88A on FP (Co-M88A-FP) catalyst. The effects of *in situ* synthesis on FP and subsequent Co doping on the physical/chemical properties of the MIL-88A were examined using scanning electron microscopy and various spectroscopies. In batchwise and continuous flow experiments, the Co-M88A-FP/PMS system demonstrated excellent RhB removal capability, for which the influencing factors and possible mechanisms were investigated.

2. Materials and methods

2.1 Materials

Double-ring qualitative (medium-rate) FP was purchased from Stofan Biotechnology Ltd. (Hangzhou, China) and was cut to size (3 cm in diameter) before being used to prepare the MIL-88A on FP (M88A-FP) catalyst component and Co-M88A-FP catalyst. Intact pieces of the same FP (11 cm in diameter) were used to collect M88A and Co-M88A powders by gravity filtration. Rhodamine B (RhB), Congo red (CR), PMS (Oxone ($2KHSO_5{\cdot}KHSO_4{\cdot}K_2SO_4$), 98%), 1,4-benzoquinone (*p*-BQ; 99%), *tert*-butanol (TBA; 99%), L-histidine (98%), and fumaric acid (99%) were purchased from Macklin Biochemical Company (Shanghai, China). Cobalt nitrate hexahydrate ($Co(NO_3)_2{\cdot}6H_2O$, 98.5%), ferric chloride hexahydrate ($FeCl_3{\cdot}6H_2O$, 99%), sodium hydroxide (NaOH, 96%), urea (99%), and methanol (99.5%) were purchased from Sinopharm Reagent Co., Ltd. (Shanghai, China). Methyl orange (MO) and methylene blue trihydrate (MB) were purchased from Alfa Aesar (Shanghai, China). All reagents were used without further purification.

2.2 Preparation of Co-M88A-FP catalyst

The preparation of MIL-88A on filter paper (M88A-FP) was adapted from a method reported by Wang *et al.*[25] First, 10 mmol fumaric acid and 10 mmol $FeCl_3{\cdot}6H_2O$ were each dissolved in 25 mL of deionized water. A piece of cellulose FP (3 cm diameter) was immersed in the $FeCl_3{\cdot}6H_2O$ solution for 12 h at room temperature. Subsequently, the fumaric acid solution was added to the $FeCl_3{\cdot}6H_2O$ solution with FP, gently mixed, and transferred to a 100 mL Teflon-lined autoclave. The sealed autoclave was heated at 80 °C for 2 h and cooled, and the resulting M88A-FP was rinsed with deionized water, freeze-dried, and stored in a sealed plastic bag.

Using M88A-FP as the precursor, Co-M88A-FP was synthesized following a method reported by Li *et al.*[26] A 50 mL solution of $Co(NO_3)_2{\cdot}6H_2O$ (11.2 mM) and urea (27.8 mM) was added to each sample of M88A-FP placed in a 100 mL glass beaker. After covering with a watch glass and then heating in a water bath at 90 °C for 1 h, the Co-M88A-FP samples were rinsed with deionized water, freeze-dried and stored in plastic bags. The procedures used to synthesize M88A and Co-M88A powders were similar to those used for the synthesis of M88A-FP and Co-M88A-FP, respectively, except for the absence of FP. After the synthesis reactions, M88A and Co-M88A were collected by gravity filtration and washed with an excess of deionized water. Both products, still on FP, were freeze-dried to obtain dry powders; these were stored in plastic bags until needed.

2.3 Catalyst characterization methods

The morphology of the immobilized and free powder catalysts was characterized by SEM (GIMINER 300, ZEISS, Germany). The key elements (C, O, Co, and Fe) and their distributions in the Co-M88A-FP catalyst were characterized by energy-dispersive X-ray spectroscopy (EDS). The crystalline structures of the catalysts were investigated using XRD (DMAX III VC, Rigaku, Japan) with Cu-Kα radiation (λ = 1.54 Å) at 40 kV and 30 mA. Patterns were collected from 10° to 60° with a 5° min^{-1} step. The surface chemical state of each catalyst was analyzed using XPS (AXIS ULTRA DLD, Kratos, Japan). The characterization was performed at a

pressure of approximately 8×10^{-9} Pa using an Al Kα X-ray as the excitation source.

2.4 Chemical analysis methods

The concentrations of RhB were determined *via* UV-vis spectrophotometry (UV-2450, SHIMADZU, Japan). To elucidate the differences in catalytic performance, the pseudo-first-order kinetic pattern was selected to describe the catalytic degradation rate of RhB under different conditions, which is given using the following equation:

$$\ln C/C_0 = -k_{obs}t \quad (1)$$

where t is the treatment time (min); C and C_0 are the concentrations (mg L^{-1}) of RhB at $t = t$ and 0, respectively; and k_{obs} is the pseudo-first-order rate constant (min^{-1}) determined for RhB degradation.

Electron paramagnetic resonance (EPR; EMX-PLUS, Bruker, USA) was used to identify the active species in the reaction system with the Co-M88A-FP catalyst. 5,5-Dimethyl-1-pyrroline *N*-oxide (DMPO) and 2,2,6,6-tetramethylpiperidine (TEMP) were used as the spin-trapping agents. Co-M88A-FP and PMS were pre-mixed in an aqueous solution for 10 min before the spectra were collected.

The leaching of Co and Fe in the reaction mixture after the degradation reaction of RhB was determined by inductively coupled plasma mass spectrometry (ICP-MS; iCAP RQ, Thermo Scientific, USA).

The charges of the RhB solution before and after the reaction and those of the RhB + catalyst solution at different pH values were characterized using a nanoparticle size and zeta potential analyzer (BeNano 180 Zate, China).

2.5 Batchwise dye degradation experiments

In the batch experiments, the degradation reactions of RhB were performed in a 250 mL flat-bottom glass beaker. Typically, 200 mL of a 20 mg L^{-1} RhB solution was adjusted to the desired initial pH with 0.1 M sulfuric acid and 0.1 M sodium hydroxide using a mechanical stirrer at a pre-set temperature (25 °C, 35 °C, or 45 °C). Then, given amounts of the catalyst (50, 75, 100, 125, or 150 mg L^{-1}) and PMS (40, 60, 80, 100, or 120 mg L^{-1}) were added to the RhB solution to start the degradation reaction. A 3 mL aliquot of the dye-containing solution was withdrawn at each selected sampling time (2, 5, 7, 10, 12, 15, 17, and 20 min), filtered through a 0.22 μm PTFE filter, and analyzed using the UV-vis spectrophotometer. Experimental conditions held constant are shown in parentheses for determinations of the effects of the Co-M88A-FP dosage (25 °C, 100 mg L^{-1} PMS, pH = 5), PMS concentration (25 °C, 100 mg L^{-1} Co-M88A-FP, pH = 5), temperature (100 mg L^{-1} Co-M88A-FP, 100 mg L^{-1} PMS, pH = 5) and initial pH of the reaction medium (25 °C, 100 mg L^{-1} Co-M88A-FP, 100 mg L^{-1} PMS) on RhB degradation. The catalytic dose is the total mass of the filter paper and MOF material loaded on it. Additional dyes (CR, MB, and MO) were subjected to batchwise degradation reactions using the same procedure. The maximum absorption wavelengths of RhB, CR, MB, and MO were 554, 496, 665, and 465 nm, respectively.[27–30]

The stability and reusability of Co-M88A-FP catalyst were evaluated using four consecutive cycles. The used catalyst was collected after each cycle, washed three times with deionized water, dried at 40 °C for 24 h, and used for the next run. The ROS formed in the Co-M88A-FP/PMS system were determined by using MeOH (100 mM), TBA (100 mM), *p*-BQ (20 mM), and L-histidine (5 mM) as radical scavengers. All batchwise tests were performed in triplicate.

2.6 Dye degradation experiments under continuous flow

Fig. 1 provides a diagram of the experimental equipment in a flow-type setup. For testing the degradation reaction under a continuous flow, a piece of Co-M88A-FP was placed at the bottom of a sintered glass funnel. Using a peristaltic pump, the RhB solution (20 mg L^{-1}) and PMS solution (100 mg L^{-1}) were introduced at flow rates of 6 or 12 mL h^{-1}. Filtrates were collected every hour using a fraction collector over a 72 h period. A 3 mL aliquot of each sample was filtered through a 0.22 μm PTFE filter before analysis by UV spectrometry to determine the RhB concentration. The liquid flux was calculated using the following equation:

$$\text{Flux}\left(\text{L m}^{-2}\text{ h}^{-1}\right) = \frac{V}{S \times T} \quad (2)$$

where V represents the volume (L) of the treated liquid, S is the effective area (m^2) of the catalyst and T is the time (h).

3. Results and discussion

3.1 Characterization of the catalyst components and catalysts

The XRD patterns of catalyst components and catalysts are shown in Fig. 2. The XRD peaks of M88A were located at 2θ = 8.0°, 10.5° and 13.3°, which are in agreement with previous reports, confirming that M88A was successfully synthesized.[31] We attribute the lower intensity of the XRD

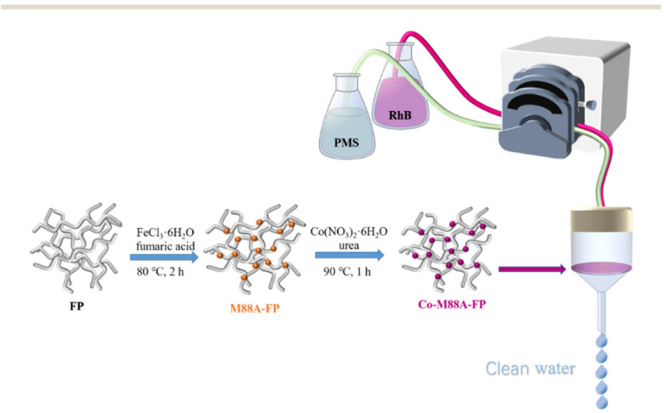

Fig. 1 Schematic of the preparation of Co-M88A-FP catalyst and its application in the continuous treatment of wastewater with a flow-type setup.

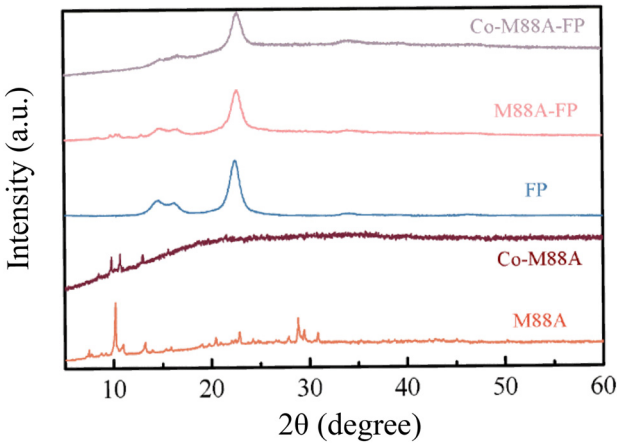

Fig. 2 XRD patterns of the catalyst components (M88A, FP, and M88A-FP) and catalysts (Co-M88A and Co-M88A-FP).

peaks of Co-M88A to the reaction of Co^{2+} on the MOF surface during the Co doping process, which may have generated protons that eroded M88A, giving rise to a more porous and amorphous structure.[26] The characteristic peaks at 2θ = 14.7°, 16.5°, 22.7°, and 34.2° corresponded to the (−1 1 0), (1 1 0), (2 0 0), and (0 0 4) lattice planes of cellulose I, respectively.[32] When the FP was loaded with M88A or Co-M88A, the cellulose peak was still clearly present in the XRD patterns, but the characteristic peaks of M88A and Co-M88A were not easily observed owing to the predominance of the cellulose peaks.[33]

The morphologies of the catalyst components and catalysts were characterized by SEM, and the images are shown in Fig. 3. The morphology of the pure M88A was typical, that is, hexagonal microrods with an average length of 2.5 μm (Fig. 3a).[29] However, the addition of cobalt resulted in the crystal surface becoming rough and amorphous, which is consistent with the XRD results (Fig. 3b). Fig. 3c clearly shows that the hexahedral structure of M88A remained unchanged after M88A was loaded on the FP and dispersed on cellulose fibers (Fig. 3c). This result demonstrates that the crystal growth of M88A is not affected by the presence of FP during the *in situ* synthesis. As shown in Fig. 3(d), the Co-M88A-FP catalyst had a more amorphous appearance than M88A-FP, likely due to the Co loading on the surface of M88A in the form of small particles and interactions with the fibers. The catalyst Co-M88A-FP was subjected to EDS analysis to further explore its elemental distribution. Results confirm that the Co-M88A-FP catalyst shows the presence of Co, Fe, C, and O and that these elements are uniformly distributed on the catalyst surface (Fig. 3e1–e4).

The XPS survey scans showed the presence of the expected elements (C, O, and Fe) on M88A and M88A-FP catalyst components (Fig. 4a); the characteristic peak for Co was apparent in the XPS spectrum of Co-M88A-FP catalyst, demonstrating the successful doping of Co on M88A-FP. Fig. 4b displays the Fe 2p spectra of the catalyst components (M88A and M88A-FP) and Co-M88A-FP catalyst. The XPS spectra of Fe 2p for M88A and M88A-FP could be divided into Fe $2p_{3/2}$ (711.53/711.93 eV) and Fe $2p_{1/2}$ (725.33/725.53 eV), with satellite signals at 717.17 and 717.83 eV. The peak

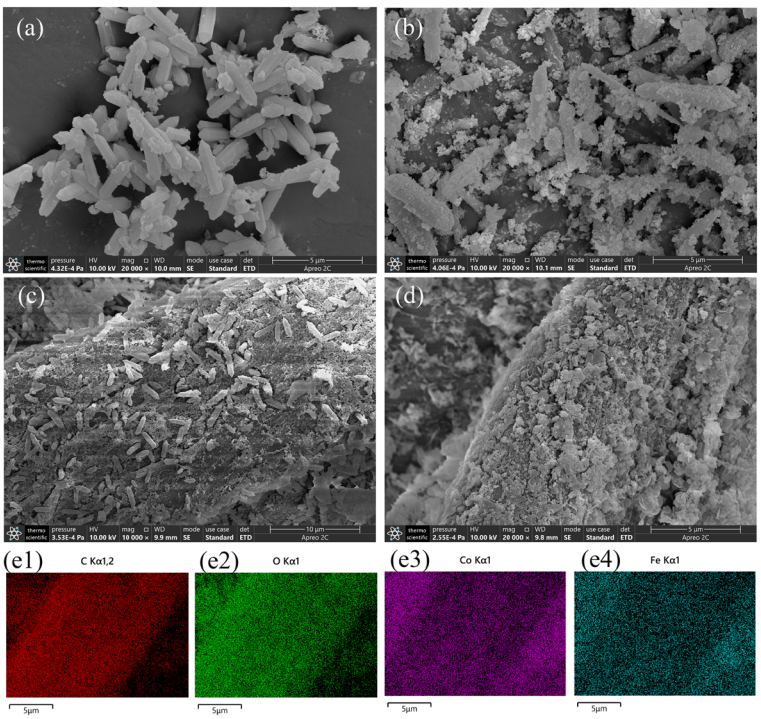

Fig. 3 SEM images of (a) M88A, (b) Co-M88A, (c) M88A-FP, and (d) Co-M88A-FP. Elemental mapping images of (e1) C, (e2) O, (e3) Co and (e4) Fe in Co-M88A-FP.

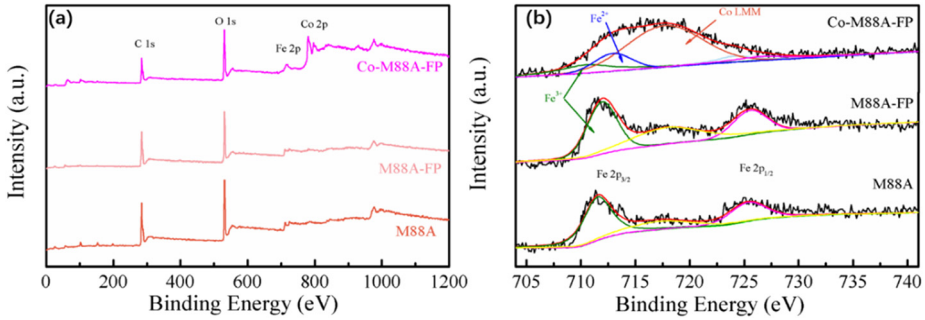

Fig. 4 XPS spectra of M88A, M88A-FP and Co-M88A-FP: (a) survey and (b) Fe 2p spectra.

distance between Fe $2p_{3/2}$ and Fe $2p_{1/2}$ was about 13.6 eV, which is close to that reported for Fe_2O_3,[34] thereby showing that Fe^{3+} is present in M88A and M88A-FP. After doping with Co, the Fe 2p spectrum showed extra peaks representing Fe^{2+} at 712.9 eV and 717.6 eV; however, the peak at 717.6 also corresponded to the Auger electron peak of Co.[35] This phenomenon is consistent with the XRD and SEM results, all of which are strong evidence of the successful cobalt loading.

3.2 Performance of Co-M88A-FP catalyst in batchwise experiments

The catalytic activity of Co-M88A-FP was assessed by calculating the degradation efficiency of RhB (Fig. 5). In the absence of PMS, very little RhB was removed by the Co-M88A-FP catalyst. Similarly, using FP and M88A-FP, very little RhB was removed, thereby indicating that the effect of RhB adsorption in subsequent experiments would be negligible. Another control analysis was performed using PMS without the Co-M88A-FP catalyst, which showed that the degradation of RhB reached only 5.06% after 20 min, thereby demonstrating that the oxidizing power of PMS alone is extremely limited. Furthermore, when M88A-FP was added to the RhB solution with PMS, only a limited degradation of RhB (*ca.* 9.06%) was observed. Notably, the use of Co-M88A-FP catalyst in the reaction system resulted in a dramatic increase in the degradation efficiency, in which the full degradation of RhB could be achieved within 20 min. This result clearly demonstrates that cobalt doping significantly enhances the catalytic activation of PMS.

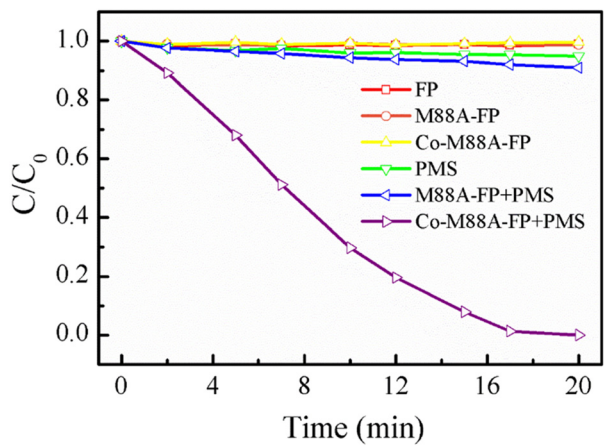

Fig. 5 Concentrations of RhB as a function of time in different systems (reaction conditions: 25 °C; 100 mg L^{-1} PMS; 100 mg L^{-1} Co-M88A-FP catalyst; 20 mg L^{-1} RhB; and pH_0 = 5).

Intuitively, the catalyst dosage should be limited within a reasonable range and preferably optimized to achieve a satisfactory catalytic effect using the least amount, thereby reducing costs and the possibility of secondary pollution caused by any metal-ion leaching from the catalyst. As shown in Fig. 6a, when the Co-M88A-FP catalyst dosage was 50 mg L^{-1}, 90.94% of RhB could be degraded within 20 min. The degradation rate of RhB reached 100% when the catalyst dosage was 100 mg L^{-1} or higher. The degradation of RhB and k_{obs} gradually increased with an increase in the catalyst dosage, which is attributable to the presence of more active sites. In addition, the k_{obs} was positively related to the catalyst dosage in the range of 50–150 mg L^{-1} (Fig. 6a1). Based on the above results, a 100 mg L^{-1} Co-M88A-FP dosage was selected for the subsequent batchwise experiments to assess the impacts of PMS concentration, temperature, and pH.

The effect of the PMS concentration on RhB degradation is shown in Fig. 6b and b1, where the RhB degradation rate increased from 73.63% to 100% and the k_{obs} increased from 0.068 min^{-1} to 0.164 min^{-1} as the PMS concentration increased from 40 mg L^{-1} to 100 mg L^{-1}. However, the *k*-value remained almost constant when the PMS concentration was further increased to 120 mg L^{-1}, indicating that PMS may have saturated the available active sites on the Co-M88A-FP catalyst.

Temperature is known to be a critical factor for SR-AOPs.[36] Fig. 6c demonstrates the removal of RhB at three different temperatures. Coinciding with the increase in temperature was a significant increase in the RhB degradation rate. In addition, the k_{obs} increased from 0.164 min^{-1} at 25 °C to 0.286 min^{-1} at 35 °C and then to 0.432 min^{-1} at 45 °C. The correlation between the temperature and rate constant was further fitted with the Arrhenius equation (eqn (2)); the apparent activation energy was determined to be 38.13 kJ mol^{-1} (Fig. S1†). The catalytic activity of Co-M88A-FP catalyst for our target pollutant (RhB) was higher compared to other

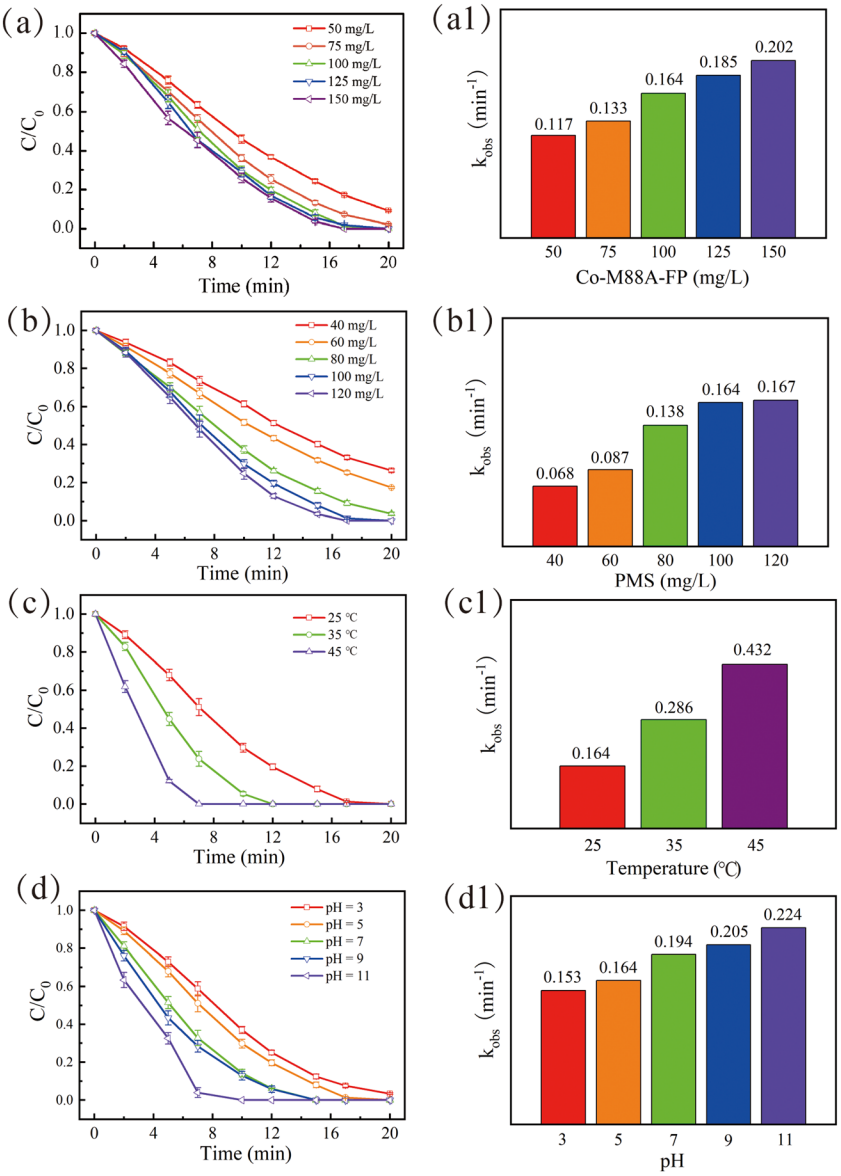

Fig. 6 Effects of (a) Co-M88A-FP catalyst dosage, (b) PMS concentration, (c) temperature, and (d) initial pH on RhB degradation (a1, b1, c1, and d1 are the k_{obs} values of the corresponding degradation reactions; reaction conditions: 25 °C; 100 mg L^{-1} PMS; 100 mg L^{-1} Co-M88A-FP catalyst; 20 mg L^{-1} RhB; and pH_0 = 5).

similar catalytic systems with higher apparent activation energies for other water pollutants.[37,38]

$$\ln k_{obs} = -\frac{E_a}{RT} + A \quad (3)$$

E_a, R, T, k_{obs}, t, and A represent the activation energy of the reaction, the gas constant, the temperature of the reaction system, the reaction rate constant, the reaction time and the temperature-independent constant, respectively.

The initial pH of a system is known to exert a profound effect on the removal of organic pollutants, including RhB.[39] Fig. 6d shows that the efficiency of RhB degradation under acidic conditions (pH = 3 or 5) was lower than that at neutral pH. This was caused by the hydrogen bonds formed between the H^+ and O–O of HSO_5^- under acidic conditions, which hampered HSO_5^- interactions with the positive charge carried by the oxide surface.[40] In addition, H^+ could stabilize HSO_5^- and scavenge $SO_4^{\bullet-}$ and $^{\bullet}OH$, thus reducing the degradation activity.[41] The degradation rate of RhB improved significantly when the solution pH was increased from 7 to 11, which is attributed to weaker hydrogen bonding between PMS and the Co-M88A-FP catalyst as well as the increased production of $SO_4^{\bullet-}$ and $^{\bullet}OH$. Although the RhB degradation rate varies with the pH, the results show that the Co-M88A-FP/PMS system is robust, maintaining good activity in the pH range from 3 to 11. Thus, wastewaters over a wide pH range can be effectively treated using the Co-M88A-FP/PMS system, with cost savings compared to other catalysts necessitating chemical additions

to adjust the wastewater pH.[42] The zeta potential values of RhB solutions at different pH values were determined and analyzed, and the results are listed in Fig. S2.† It can be seen that the RhB solution displays a positive charge at a pH value lower than 5 owing to the tertiary amine cations on RhB under acidic conditions.[43]

Additionally, the negative charge of the RhB solution at a pH higher than 5 was attributed to the deprotonated carboxyl group of RhB under basic conditions.[43] When the catalyst Co-M88A-FP was added to the RhB solution (*i.e.*, no PMS was added to avoid the influence from degradation intermediates), the solution remained electronically neutral at most pH values, except for being positively charged at a pH of 3 and negatively charged at a pH of 11. The zeta potential values of the RhB solution after degradation were close to 0 at most pH values except for a pH of 11, suggesting that the degradation products were mostly electronically neutral. The above results imply that the effect of the pH value of the reaction medium on the degradation of RhB is complicated. It has been reported that in addition to affecting the adsorption of the pollutant onto the catalyst, the pH value of the reaction medium also affects the reaction pathway of the degradation of the pollutant, which is RhB in this study.[44,45]

Robust catalyst systems not only demand efficient catalytic performance but also demand catalyst reusability and stability. The next step in our evaluation of Co-M88A-FP catalyst was to subject it to successive RhB removal experiments under the same conditions. Fig. 7 shows the performance of the catalyst during four RhB degradation cycles. The degradation curves were similar for the four cycles, and the RhB degradation rate was maintained at 88.84% in the fourth cycle. We ascribe this slight decrease to the leaching of small amounts of Co^{2+}. It should be noted that the leaching of Co^{2+} in the solution after the first reaction was 121.4 μg L^{-1}, which is much lower than 'the wastewater discharge standards in China (GB 25467–2010) (1 mg L^{-1})'.[46]

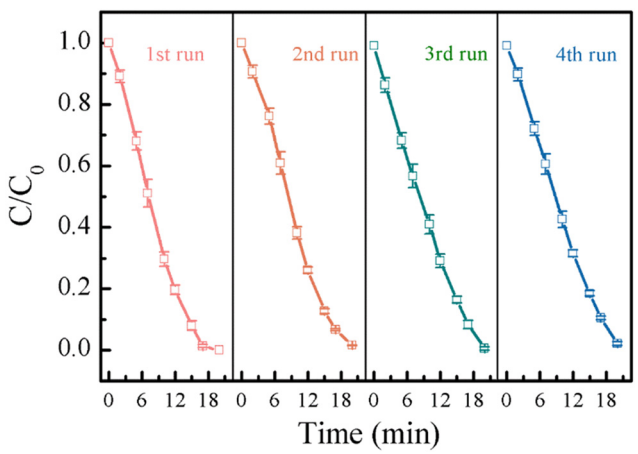

Fig. 7 Reusability of Co-M88A-FP catalyst for the degradation of RhB (reaction conditions: 25 °C; 100 mg L^{-1} PMS; 100 mg L^{-1} Co-M88A-FP catalyst; 20 mg L^{-1} RhB; and pH_0 = 5).

Overall, these results confirm that the Co-M88A-FP catalyst possesses the efficiency and long-term stability essential for practical wastewater treatment applications.

3.3 Performance of Co-M88A-FP catalyst under continuous flow

The catalytic performance of Co-M88A-FP catalyst was measured under continuous flow to make use of its inherent property of having a pore structure capable of allowing liquids to flow through it. A schematic diagram of the flow-type reactor allowing continuous flow is provided in Fig. 1. The catalytic reaction can be completed under continuous flow when a peristaltic pump is used to steadily pump PMS and RhB solutions through the device. The degradation efficiency of RhB remained at 100% throughout the catalytic degradation reaction over 72 h at a flow rate of 6 mL h^{-1}, indicating the efficient and stable catalytic activity of Co-M88A-FP catalyst. When the flow rate was doubled (12 mL h^{-1}), the removal efficiency remained approximately 100% for the first 12 h. Then, the RhB degradation efficiency decreased to 77% after 53 h and remained at this level until the reaction was complete at 72 h. The liquid fluxes corresponding to flow rates of 6 ml L^{-1} and 12 ml L^{-1} were 8.5 L m^{-2} h^{-1} and 17.0 L m^{-2} h^{-1}, respectively.

The XPS spectra of the virgin Co-M88A-FP catalyst and Co-M88A-FP catalyst obtained after 20 min of use in the batchwise reaction were compared to evaluate the stability of individual elements and selected functional groups. The XPS spectra for the Co-M88A-FP catalysts before and after use were essentially the same (Fig. 8a). As shown in Fig. 8b, compared to the fresh Co-M88A-FP catalyst, the percentage of Fe^{3+} decreased from 49.65% to 41.98% and the percentage of Fe^{2+} increased from 50.35% to 58.02%, indicating a change in the valence state of Fe. Fig. 8c shows peaks at 780.59/795.99 eV and 782.34/797.74 eV, which are associated with Co^{2+} and Co^{3+}, respectively. Similarly, the relative contents of Co^{2+} and Co^{3+} changed from 55.87% and 44.13% to 51.86% and 48.14%, respectively. We attribute this change to an electron transfer reaction with Co during PMS activation. The XPS spectra of O 1s are presented in Fig. 8d. The five peaks with binding energies of 533.42 eV, 532.84 eV, 532.24 eV, 531.52 eV and 530.01 eV were attributed to the C–O and O–C═O bonds of the FP, the oxygen component on the carboxylate group of the fumarate, the O–H bond of the surface hydroxyl group, and the lattice oxygen (O_{latt}), respectively.[47,48] The hydroxyl content changed after the catalyst use, increasing from 22.53% to 30.81%, probably due to the generation of Co–OH and Fe–OH functionalities.

The ROS during the degradation reaction were investigated using EPR, DMPO and TEMP were selected as trapping agents. A set of peak signals with intensities of 1 : 2 : 2 : 1 was detected in the reaction solution when DMPO was used as a trapping agent, which could be attributed to DMPO–$^{\bullet}OH$ and DMPO–$SO_4^{\bullet-}$ signals, as shown in Fig. 9a.

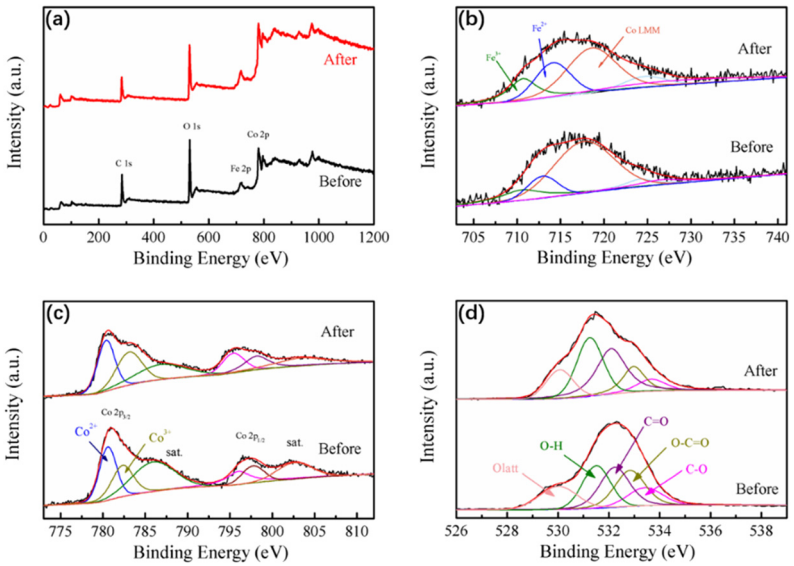

Fig. 8 XPS spectra of Co-M88A-FP catalyst before and after use: (a) full-range scan, (b) Fe 2p, (c) Co 2p and (d) O 1s spectra.

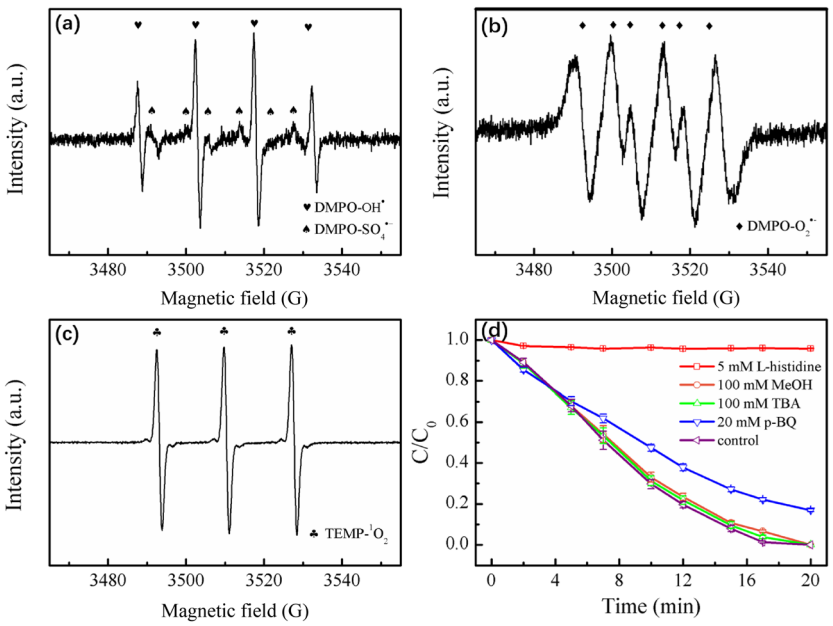

Fig. 9 EPR spectra with DMPO (a and b) and TEMP (c) as the trapping agents. (d) Effects of different radical scavengers on RhB degradation (reaction conditions: 25 °C; 100 mg L^{-1} PMS; 100 mg L^{-1} Co-M88A-FP catalyst; 20 mg L^{-1} RhB; and pH_0 = 5).

The DMPO–$O_2^{\bullet-}$ signal is shown in Fig. 9b, indicating the production of $SO_4^{\bullet-}$, $^{\bullet}OH$ and $O_2^{\bullet-}$ in the Co-M88A-FP/PMS system. The triple peak characteristic of $^1O_2$ captured by TEMP was apparent and had a high peak intensity (Fig. 9c), demonstrating that $^1O_2$ was present in the Co-M88A-FP/PMS system.

The presence of different ROS was confirmed by radical scavenging experiments, wherein TBA, MeOH, *p*-BQ and L-histidine were selected to scavenge $^{\bullet}OH$, $SO_4^{\bullet-}$, $O_2^{\bullet-}$ and $^1O_2$, respectively. Fig. 9d shows that 100 mM TBA or 100 mM MeOH had little effect on the degradation of RhB, with the dye being close to completely degraded at 20 min. The RhB degradation efficiency dropped to 83.04% when 20 mM *p*-BQ was added to the Co-M88A-FP/PMS system, indicating that $O_2^{\bullet-}$ played some role in the degradation reaction. Finally, the degradation rate of RhB markedly decreased to 4.12% after 5 mM L-histidine was added to the reaction mixture, indicating that $^1O_2$ played a significant role in the degradation of RhB. According to this, the degradation of RhB was dominated by $^1O_2$ in the Co-M88A-FP/PMS system, while $O_2^{\bullet-}$, $^{\bullet}OH$ and $SO_4^{\bullet-}$ showed little or no contribution to RhB degradation processes.[49–51]

Taking into consideration the XPS, EPR, and radical scavenging tests, the possible mechanisms of PMS activation by the Co-M88A-FP catalyst were proposed. First, PMS and Co^{2+}/Fe^{2+} undergo electron transfer on the Co-M88A-FP catalyst surface to generate Co^{3+} and $SO_4^{\bullet-}$ (eqn (4) and (5)).[52,53] Then, $SO_4^{\bullet-}$ is transformed into HSO_4^- and generates $^{\bullet}OH$ at the same time (eqn (6)). In addition, Co^{2+} can be obtained as Co^{3+} reacts with HSO_5^- again, achieving the cycle between Co^{2+} and Co^{3+} (eqn (7)).[54] However, upon comparison of the redox potential of $HSO_5^-/SO_5^{\bullet-}$ (1.10 V), Fe^{3+}/Fe^{2+} (0.77 V) and $O_2^{\bullet-}/O_2$ (−0.33 V), the Fe^{3+}/Fe^{2+} cycle is more likely to be achieved by $O_2^{\bullet-}$ (eqn (8)).[55–57] Two mechanisms are proposed for $O_2^{\bullet-}$ formation from dissolved oxygen and the decomposition of PMS (eqn (9) and (10)).[58,59] $O_2^{\bullet-}$ is further transformed into $^1O_2$ and H_2O_2 by reacting with H_2O (eqn (11)).[60] Finally, alternative pathways for the formation of $^1O_2$ may be the autolysis of $SO_5^{\bullet-}$ or the direct reaction with Co^{2+}/Fe^{2+} (eqn (12)–(14)).[61] It has been reported that RhB is mainly degraded to low or non-toxic intermediates, including carboxylic acids, dicarboxylic acids, amine compounds, and inorganic ions, *via* processes such as the de-ethylation at the *n*-position, breakage of the chromophore, and cleavage of the benzene ring.[45,62–65]

$$Co^{2+} + HSO_5^- \rightarrow Co^{3+} + SO_4^{\bullet-} + OH^- \quad (4)$$

$$Fe^{2+} + HSO_5^- \rightarrow Fe^{3+} + SO_4^{\bullet-} + OH^- \quad (5)$$

$$SO_4^{\bullet-} + OH^- \rightarrow SO_4^{2-} + {}^{\bullet}OH \quad (6)$$

$$Co^{3+} + HSO_5^- \rightarrow Co^{2+} + SO_5^{\bullet-} + H^+ \quad (7)$$

$$Fe^{3+} + O_2^{\bullet-} \rightarrow Fe^{2+} + O_2 \quad (8)$$

$$HSO_5^- + H_2O \rightarrow O_2^{\bullet-} + SO_4^{2-} + 2H^+ \quad (9)$$

$$O_2 + e^- \rightarrow O_2^{\bullet-} \quad (10)$$

$$2O_2^{\bullet-} + 2H_2O \rightarrow {}^1O_2 + H_2O_2 + 2OH^- \quad (11)$$

$$2SO_5^{\bullet-} \rightarrow 2SO_4^{\bullet-} + {}^1O_2 \quad (12)$$

$$2Co^{2+} + 2SO_5^- \rightarrow 2Co^{3+} + 2SO_4^{2-} + {}^1O_2 \quad (13)$$

$$2Fe^{2+} + 2SO_5^- \rightarrow 2Fe^{3+} + 2SO_4^{2-} + {}^1O_2 \quad (14)$$

The degradation performance of the Co-M88A-FP/PMS system with different anionic and cationic dyes (see Fig. S3†) verified its utility for treating a variety of wastewater streams. Congo red and methyl orange were completely degraded within 7 and 20 min, respectively, while the degradation rate of methylene blue was only 59.15% at 20 min. Intuitively, this may be due to the presence of different substituents in different dyes affecting the activity of the reaction. The dominant ROS in the Co-M88A-FP/PMS system is $^1O_2$, which is reported to react with electron-rich groups, such as $-CH_3$, $-NH_2$ and $-NR_2$.[66,67] Even though methylene blue also has electron-rich substituents, the two methyl groups bonded to N have significant steric hindrance, resulting in a reduction in reactivity.[68] Therefore, electron-rich substances with low steric hindrance would be degraded more quickly in the Co-M88A-FP/PMS system.

Finally, the degradation efficiency of Co-M88A-FP catalyst prepared in this study was compared with those of the other reported MOF catalysts used to degrade RhB (Table S1†).[69–74] This comparison clearly demonstrates that our Co-M88A-FP catalyst has excellent degradation performance.

4. Conclusion

This study demonstrated the promising application of a cobalt-doped MIL-88A/cellulose catalyst for the activation of PMS to degrade dyes found in wastewaters. Filter paper, as a carrier for the MOF, avoided aggregation of the MOF and facilitated catalyst separation and recovery. The presence of Co and Fe ions promoted the cycling of electrons, which in turn generated more ROS, dominated by $^1O_2$. The degradation of RhB reached 100% under the optimized conditions and was maintained close to 90% for four consecutive cycles. By anchoring the MOF on a filter paper carrier, we were able to demonstrate a system amenable to continuous wastewater treatment, with RhB degradation efficiencies of 100% being achieved in a flow-type setup. In conclusion, this study provides further insight into the design of MOF-based catalysts for the treatment of dyes in wastewater. Later, the application of this catalyst will be expanded to study the degradability of pollutants and its anti-interference performance in treating complex aqueous systems (real wastewater).

Data availability

The research data of the current work will be available upon request.

Conflicts of interest

There are no conflicts to declare.

Acknowledgements

The authors are grateful for the financial support from the National Natural Science Foundation of China (No. 31770631). Advanced analysis and testing center of Nanjing Forestry University is also acknowledged.

References

1 B. L. Alderete, J. da Silva, R. Godoi, F. R. da Silva, S. R. Taffarel, L. P. da Silva, A. L. H. Garcia, H. M. Júnior, H. L. N. de Amorim and J. N. Picada, Evaluation of toxicity and mutagenicity of a synthetic effluent containing azo dye after Advanced Oxidation Process treatment, *Chemosphere*, 2021, **263**, 128291.

2 Z. Li, X. Tang, G. Huang, X. Luo, D. He, Q. Peng, J. Huang, M. Ao and K. Liu, Bismuth MOFs based hierarchical Co_3O_4-Bi_2O_3 composite: An efficient heterogeneous peroxymonosulfate activator for azo dyes degradation, *Sep. Purif. Technol.*, 2020, **242**, 116825.
3 B. Lellis, C. Z. Fávaro-Polonio, J. A. Pamphile and J. C. Polonio, Effects of textile dyes on health and the environment and bioremediation potential of living organisms, *Biotechnol. Res. Innov.*, 2019, **3**, 275–290.
4 A. Tkaczyk, K. Mitrowska and A. Posyniak, Synthetic organic dyes as contaminants of the aquatic environment and their implications for ecosystems: A review, *Sci. Total Environ.*, 2020, **717**, 137222.
5 Y. Jiao, C. Wan, W. Bao, H. Gao, D. Liang and J. Li, Facile hydrothermal synthesis of Fe_3O_4@cellulose aerogel nanocomposite and its application in Fenton-like degradation of Rhodamine B, *Carbohydr. Polym.*, 2018, **189**, 371–378.
6 C. Gong, F. Chen, Q. Yang, K. Luo, F. Yao, S. Wang, X. Wang, J. Wu, X. Li, D. Wang and G. Zeng, Heterogeneous activation of peroxymonosulfate by Fe-Co layered doubled hydroxide for efficient catalytic degradation of Rhoadmine B, *Chem. Eng. J.*, 2017, **321**, 222–232.
7 Y. Gong, X. Zhao, H. Zhang, B. Yang, K. Xiao, T. Guo, J. Zhang, H. Shao, Y. Wang and G. Yu, MOF-derived nitrogen doped carbon modified g-C_3N_4 heterostructure composite with enhanced photocatalytic activity for bisphenol A degradation with peroxymonosulfate under visible light irradiation, *Appl. Catal., B*, 2018, **233**, 35–45.
8 G. X. Huang, C. Y. Wang, C. W. Yang, P. C. Guo and H. Q. Yu, Degradation of bisphenol a by peroxymonosulfate catalytically activated with $Mn_{1.8}Fe_{1.2}O_4$ Nanospheres: Synergism between Mn and Fe, *Environ. Sci. Technol.*, 2017, **51**, 12611–12618.
9 F. Wu, H. Huang, T. Xu, W. Lu, N. Li and W. Chen, Visible-light-assisted peroxymonosulfate activation and mechanism for the degradation of pharmaceuticals over pyridyl-functionalized graphitic carbon nitride coordinated with iron phthalocyanine, *Appl. Catal., B*, 2017, **218**, 230–239.
10 H. B. Sales, R. R. Menezes, G. A. Neves, J. J. N. de Souza, J. M. Ferreira, L. Chantelle, A. L. M. de Oliveira and H. d. L. Lira, Development of sustainable heterogeneous catalysts for the photocatalytic treatment of effluents, *Sustainability*, 2020, **12**, 7393.
11 G. Wei, X. Liang, Z. He, Y. Liao, Z. Xie, P. Liu, S. Ji, H. He, D. Li and J. Zhang, Heterogeneous activation of Oxone by substituted magnetites Fe_3-xMxO_4 (Cr, Mn, Co, Ni) for degradation of Acid Orange II at neutral pH, *J. Mol. Catal. A: Chem.*, 2015, **398**, 86–94.
12 S. Yu, Q. Zhang, X. Sun, S. Chen, J. Tang, J. J. Zhu and Y. Dang, Doping Sb into $CuFe_2O_4$improved the catalytic performance in the electrochemically enhanced homogeneous peroxymonosulfate-heterogeneous catalytic system for the degradation of ciprofloxacin, *J. Environ. Chem. Eng.*, 2022, **10**, 108335.
13 J. R. Long and O. M. Yaghi, The pervasive chemistry of metal-organic frameworks, *Chem. Soc. Rev.*, 2009, **38**, 1213–1214.
14 D. Huang, G. Zhang, J. Yi, M. Cheng, C. Lai, P. Xu, C. Zhang, Y. Liu, C. Zhou, W. Xue, R. Wang, Z. Li and S. Chen, Progress and challenges of metal-organic frameworks-based materials for SR-AOPs applications in water treatment, *Chemosphere*, 2021, **263**, 127672.
15 K. Y. A. Lin, H. A. Chang and C. J. Hsu, Iron-based metal organic framework, MIL-88A, as a heterogeneous persulfate catalyst for decolorization of Rhodamine B in water, *RSC Adv.*, 2015, **5**, 32520–32530.
16 Y. Zhang, J. Zhou, X. Chen, L. Wang and W. Cai, Coupling of heterogeneous advanced oxidation processes and photocatalysis in efficient degradation of tetracycline hydrochloride by Fe-based MOFs: Synergistic effect and degradation pathway, *Chem. Eng. J.*, 2019, **369**, 745–757.
17 W. Xiang, X. Zhang, R. Xiao and Y. Zhang, Three-dimensional porous bimetallic metal–organic framework/gelatin aerogels: A readily recyclable peroxymonosulfate activator for efficient and continuous organic dye removal, *Chin. J. Chem. Eng.*, 2024, **71**, 193–202.
18 C. Tao, K. Wu, T. Liu, S. Yang and Z. Li, One-step removal of p-arsanilic acid via constructing bifunctional Zr-CuO/α-FeOOH catalyst: Efficient peroxymonosulfate activation, cooperative oxidation and adsorption, *Chem. Eng. J.*, 2025, **512**, 162285.
19 T. Chen, T. Feng, S. Wu, X. Zhang and Y. Chen, MOF-derived FeCe@ Carbon catalysts for the efficient tetracycline degradation by activated persulfate: Preparation and mechanistic study, *J. Colloid Interface Sci.*, 2025, **685**, 1041–1055.
20 D. Masekela, T. L. Yusuf, S. A. Balogun, E. Makhado, O. I. Adeniran and K. D. Modibane, Interfacial engineering of MoS2 and bimetallic MOF hybrid for superior piezo-photocatalytic hydrogen production and wastewater treatment, *J. Alloys Compd.*, 2025, **1020**, 179304.
21 W. Da Oh, Z. Dong and T. T. Lim, Generation of sulfate radical through heterogeneous catalysis for organic contaminants removal: Current development, challenges and prospects, *Appl. Catal., B*, 2016, **194**, 169–201.
22 X. Chen, X. Qiao, D. Wang, J. Lin and J. Chen, Kinetics of oxidative decolorization and mineralization of Acid Orange 7 by dark and photoassisted Co^{2+}-catalyzed peroxymonosulfate system, *Chemosphere*, 2007, **67**, 802–808.
23 T. H. V. Luong, T. H. T. Nguyen, B. V. Nguyen, N. K. Nguyen, T. Q. C. Nguyen and G. H. Dang, Efficient degradation of methyl orange and methylene blue in aqueous solution using a novel Fenton-like catalyst of CuCo-ZIFs, *Green Process. Synth.*, 2022, **11**, 71–83.
24 J. Yang, Z. Ao, H. Wu and S. Zhang, Immobilization of chitosan-templated MnO_2 nanoparticles onto filter paper by redox method as a retrievable Fenton-like dip catalyst, *Chemosphere*, 2021, **268**, 128835.
25 J. Wang, J. Wan, Y. Ma, Y. Wang, M. Pu and Z. Guan, Metal-organic frameworks MIL-88A with suitable synthesis conditions and optimal dosage for effective catalytic

degradation of Orange G through persulfate activation, *RSC Adv.*, 2016, **6**, 112502–112511.

26 J. Li, W. Zhu, Y. Gao, P. Lin, J. Liu, J. Zhang and T. Huang, The catalyst derived from the sulfurized Co-doped metal–organic framework (MOF) for peroxymonosulfate (PMS) activation and its application to pollutant removal, *Sep. Purif. Technol.*, 2022, **285**, 120362.

27 W. Su, J. Chen, L. Wu, X. Wang, X. Wang and X. Fu, Visible light photocatalysis on praseodymium(III)-nitrate-modified TiO_2 prepared by an ultrasound method, *Appl. Catal., B*, 2008, **77**, 264–271.

28 M. Yu, S. Zhao, H. Wu and S. Asuha, Efficient removal of Congo red by magnetically separable mesoporous TiO_2 modified with γ-Fe_2O_3, *J. Porous Mater.*, 2013, **20**, 1353–1360.

29 W. T. Xu, L. Ma, F. Ke, F. M. Peng, G. S. Xu, Y. H. Shen, J. F. Zhu, L. G. Qiu and Y. P. Yuan, Metal-organic frameworks MIL-88A hexagonal microrods as a new photocatalyst for efficient decolorization of methylene blue dye, *Dalton Trans.*, 2014, **43**, 3792–3798.

30 H. Zhao, G. Zhang and Q. Zhang, MnO_2/CeO_2 for catalytic ultrasonic degradation of methyl orange, *Ultrason. Sonochem.*, 2014, **21**, 991–996.

31 T. Chalati, P. Horcajada, R. Gref, P. Couvreur and C. Serre, Optimisation of the synthesis of MOF nanoparticles made of flexible porous iron fumarate MIL-88A, *J. Mater. Chem.*, 2011, **21**, 2220–2227.

32 T. Kamal, S. B. Khan and A. M. Asiri, Synthesis of zero-valent Cu nanoparticles in the chitosan coating layer on cellulose microfibers: evaluation of azo dyes catalytic reduction, *Cellulose*, 2016, **23**, 1911–1923.

33 J. S. Wang, X. H. Yi, X. Xu, H. Ji, A. M. Alanazi, C. C. Wang, C. Zhao, Y. V. Kaneti, P. Wang, W. Liu and Y. Yamauchi, Eliminating tetracycline antibiotics matrix via photoactivated sulfate radical-based advanced oxidation process over the immobilized MIL-88A: Batch and continuous experiments, *Chem. Eng. J.*, 2022, **431**, 133213.

34 X. Li, Y. Pi, L. Wu, Q. Xia, J. Wu, Z. Li and J. Xiao, Facilitation of the visible light-induced Fenton-like excitation of H_2O_2 via heterojunction of g-C_3N_4/NH_2-Iron terephthalate metal-organic framework for MB degradation, *Appl. Catal., B*, 2017, **202**, 653–663.

35 Y. Wang, S. Wang, S. L. Zhang and X. W. Lou, Formation of Hierarchical $FeCoS_2$–CoS_2 Double-Shelled Nanotubes with Enhanced Performance for Photocatalytic Reduction of CO_2, *Angew. Chem., Int. Ed.*, 2020, **59**, 11918–11922.

36 C. Cai, H. Zhang, X. Zhong and L. Hou, Ultrasound enhanced heterogeneous activation of peroxymonosulfate by a bimetallic Fe-Co/SBA-15 catalyst for the degradation of Orange II in water, *J. Hazard. Mater.*, 2015, **283**, 70–79.

37 B. Liu, W. Song, H. Wu, Y. Xu, Y. Sun, Y. Yu, H. Zheng and S. Wan, Enhanced oxidative degradation of norfloxacin using peroxymonosulfate activated by oily sludge carbon-based nanoparticles $CoFe_2O_4$/OSC, *Chem. Eng. J.*, 2020, **400**, 125947.

38 M. Xu, H. Zhou, Z. Wu, N. Li, Z. Xiong, G. Yao and B. Lai, Efficient degradation of sulfamethoxazole by $NiCo_2O_4$ modified expanded graphite activated peroxymonosulfate: Characterization, mechanism and degradation intermediates, *J. Hazard. Mater.*, 2020, **399**, 123103.

39 C. Qi, X. Liu, J. Ma, C. Lin, X. Li and H. Zhang, Chemosphere Activation of peroxymonosulfate by base : Implications for the degradation of organic pollutants, *Chemosphere*, 2016, **151**, 280–288.

40 T. Zhang, H. Zhu and J. Croue, Production of Sulfate Radical from Peroxymonosulfate Induced by a Magnetically Separable CuFe2O4 Spinel in Water: E ffi ciency, Stability, and Mechanism, *Environ. Sci. Technol.*, 2013, **47**, 2784–2791.

41 M. Cao, X. Liu and H. Yang, Facile construction of high-performance 3D Co_2C-doped $CoAl_2O_4$ fiber composites for capturing and decomposing tetracycline from aqueous solution, *J. Hazard. Mater.*, 2022, **424**, 127307.

42 D. Chen, Q. Bai, T. Ma, X. Jing, Y. Tian, R. Zhao and G. Zhu, Stable metal–organic framework fixing within zeolite beads for effectively static and continuous flow degradation of tetracycline by peroxymonosulfate activation, *Chem. Eng. J.*, 2022, **435**, 134916.

43 H. Xu, Photocatalytic rhodamine B degradation study by rare earth-doped titanium dioxide nanoparticles and synthesis of Pybox ligands, *Mphil*, Zhejiang University, China, 2006.

44 J. Du, J. Bao, X. Fu, C. Lu and S. Kim, Facile preparation of S/Fe composites as an effective peroxydisulfate activator for RhB degradation, *Sep. Purif. Technol.*, 2016, **163**, 145–152.

45 R. Su, J. Sun, Y. Sun, K. Deng, D. Cha and D. Wang, Oxidative degradation of dye pollutants over a broad pH range using hydrogen peroxide catalyzed by FePz $(dtnCl_2)_4$, *Chemosphere*, 2009, **77**, 1146–1151.

46 X. Li, Z. Liu, Y. Zhu, L. Song, Z. Dong, S. Niu and C. Lyu, Facile synthesis and synergistic mechanism of $CoFe_2O_4$@three-dimensional graphene aerogels towards peroxymonosulfate activation for highly efficient degradation of recalcitrant organic pollutants, *Sci. Total Environ.*, 2020, **749**, 141466.

47 N. Liu, W. Huang, X. Zhang, L. Tang, L. Wang, Y. Wang and M. Wu, Ultrathin graphene oxide encapsulated in uniform MIL-88A(Fe) for enhanced visible light-driven photodegradation of RhB, *Appl. Catal., B*, 2018, **221**, 119–128.

48 X. Liao, F. Wang, F. Wang, Y. Cai, Y. Yao, B.-T. Teng, Q. Hao and L. Shuxiang, Synthesis of (100) surface oriented MIL-88A-Fe with rod-like structure and its enhanced fenton-like performance for phenol removal, *Appl. Catal., B*, 2019, **259**, 118064.

49 Y. Bu, H. Li, W. Yu, Y. Pan, L. Li, Y. Wang, L. Pu, J. Ding, G. Gao and B. Pan, Peroxydisulfate activation and singlet oxygen generation by oxygen vacancy for degradation of contaminants, *Environ. Sci. Technol.*, 2021, **55**, 2110–2120.

50 S. Liu, Z. Zhang, F. Huang, Y. Liu, L. Feng, J. Jiang, L. Zhang, F. Qi and C. Liu, Carbonized polyaniline activated peroxymonosulfate (PMS) for phenol degradation: Role of PMS adsorption and singlet oxygen generation, *Appl. Catal., B*, 2021, **286**, 119921.

51 H. Fui, S. Gao, X. Ma and Y. Huang, Facile fabrication of CoAl-LDH nanosheets for efficient rhodamine B degradation via peroxymonosulfate activation, *RSC Adv.*, 2023, **13**, 29695–29705.
52 Y. Yao, Y. Cai, F. Lu, F. Wei, X. Wang and S. Wang, Magnetic recoverable $MnFe_2O_4$ and $MnFe_2O_4$-graphene hybrid as heterogeneous catalysts of peroxymonosulfate activation for efficient degradation of aqueous organic pollutants, *J. Hazard. Mater.*, 2014, **270**, 61–70.
53 L. Chen, X. Zuo, L. Zhou, Y. Huang, S. Yang, T. Cai and D. Ding, Efficient heterogeneous activation of peroxymonosulfate by facilely prepared Co/Fe bimetallic oxides: Kinetics and mechanism, *Chem. Eng. J.*, 2018, **345**, 364–374.
54 H. Li, Y. Yao, J. Zhang, J. Du, S. Xu, C. Wang, D. Zhang, J. Tang, H. Zhao and J. Zhou, Degradation of phenanthrene by peroxymonosulfate activated with bimetallic metal-organic frameworks: Kinetics, mechanisms, and degradation products, *Chem. Eng. J.*, 2020, **397**, 125401.
55 P. Neta, R. E. Huie and A. Ross, Rate Constants for Reactions of Inorganic Radicals in Aqueous Solution, *J. Phys. Chem. Ref. Data*, 1979, **17**, 1027–1284.
56 G. V. Buxton, C. L. Greenstock, W. P. Helman and A. Ross, Critical Review of rate constants for reactions of hydrated electrons, hydrogen atoms and hydroxyl radicals (·OH/·O$^-$ in Aqueous Solution), *J. Phys. Chem. Ref. Data*, 1988, **17**, 513–886.
57 Q. Wang, J. Lu, Y. Jiang, S. Yang, Y. Yang and Z. Wang, FeCo bimetallic metal organic framework nanosheets as peroxymonosulfate activator for selective oxidation of organic pollutants, *Chem. Eng. J.*, 2022, **443**, 136483.
58 L. Wu, Y. Yu, Q. Zhang, J. Hong, J. Wang and Y. She, A novel magnetic heterogeneous catalyst oxygen-defective $CoFe_2O_4$–x for activating peroxymonosulfate, *Appl. Surf. Sci.*, 2019, **480**, 717–726.
59 W. Qin, G. Fang, Y. Wang and D. Zhou, Mechanistic understanding of polychlorinated biphenyls degradation by peroxymonosulfate activated with $CuFe_2O_4$ nanoparticles: Key role of superoxide radicals, *Chem. Eng. J.*, 2018, **348**, 526–534.
60 G. Liu, H. Yu, T. Zhou, R. Jin and J. Zhou, Activation of peroxydisulfate by biogenic nanocomposites of reduced graphene oxide and goethite for non-radical selective oxidation of organic contaminants: Production of singlet oxygen and direct electron transfer, *Chem. Eng. J.*, 2022, **430**, 133177.
61 H. Li, J. Zhang, Y. Yao, X. Miao, J. Chen and J. Tang, Nanoporous bimetallic metal-organic framework (FeCo-BDC) as a novel catalyst for efficient removal of organic contaminants, *Environ. Pollut.*, 2019, **255**, 113337.
62 Z. Diao, J. Liu, Y. Hu, L. Kong, D. Jiang and X. Xu, Comparative study of Rhodamine B degradation by the systems pyrite/H_2O_2 and pyrite/persulfate: reactivity, stability, products and mechanism, *Sep. Purif. Technol.*, 2017, **184**, 374–383.
63 P. Liu, D. Zhong, Y. Xu and N. Zhong, Nitrogen doped Cu/Fe@ PC derived from metal organic frameworks for activating peroxymonosulfate to degrade Rhodamine, *J. Environ. Chem. Eng.*, 2022, **10**, 107595.
64 H. Cui, H. Huang, B. Yuan and M. Fu, Decolorization of RhB dye by manganese oxides: effect of crystal type and solution pH, *Geochem. Trans.*, 2015, **16**, 1–8.
65 K. Bera, M. Chakraborty, M. Mondal, S. Banlk and S. Bhattacharya, Synthesis of α-β Bi_2O_3 heterojunction photocatalyst and evaluation of reaction mechanism for degradation of RhB dye under natural sunlight, *Ceram. Int.*, 2022, **46**, 7667–7680.
66 G. Li, X. Q. Cao, N. Meng, Y. M. Huang, X. D. Wang, Y. Y. Gao, X. Li, T. S. Yang, B. L. Li, Y. Z. Zhang, X. J. Lyu and Y. Liang, Fe_3O_4 supported on water caltrop-derived biochar toward peroxymonosulfate activation for urea degradation: the key role of sulfate radical, *Chem. Eng. J.*, 2022, **433**, 133595.
67 J. Xiao, Y. Xie, Q. Han, H. Cao, Y. Wang, F. Nawaz and F. Duan, Superoxide radical-mediated photocatalytic oxidation of phenolic compounds over Ag^+/TiO_2: Influence of electron donating and withdrawing substituents, *J. Hazard. Mater.*, 2016, **304**, 126–133.
68 Z. Ma, Q. Jia, C. Tao and B. Han, Highlighting unique function of immobilized superoxide on TiO_2 for selective photocatalytic degradation, *Sep. Purif. Technol.*, 2020, **238**, 116402.
69 Z. Yu, X. Hu and Z. Su, Activation of peroxymonosulfate by a novle stratiform Co-MOF as catalyst for degradation of dyes in water, *J. Mol. Struct.*, 2024, **1296**, 136787.
70 W. Zhu, M. Han, D. Kim, J. Park, H. Choi, G. Kwon, J. You, S. Li, T. Park and J. Kim, Highly catalytic and durable nanocellulose fibers-based nanoporous membrane film for efficient organic pollutant degradation, *J. Water Process Eng.*, 2023, **53**, 103620.
71 E. Amdeha and R. Mohamed, A green synthesized recyclable ZnO/MIL-101 (Fe) for Rhodamine B dye removal via adsorption and photo-degradation under UV and visible light irradiation, *Environ. Technol.*, 2021, **42**, 842–859.
72 L. Hu, G. Deng, W. Lu, Y. Lu and Y. Zhang, Peroxymonosulfate activation by Mn_3O_4/metal-organic framework for degradation of refractory aqueous organic pollutant rhodamine B, *Chin. J. Catal.*, 2017, **38**, 1360–1372.
73 P. Liu, D. Zhong, Y. Xu, N. Zhong and G. He, Co/Fe co-doped porous graphite carbon derived from metal organic framework for microelectrolysis-Fenton catalytic degradation of Rhodamine B, *J. Environ. Chem. Eng.*, 2021, **9**, 105924.
74 W. Zhu, M. Han, D. Kim, Y. Zhang, G. Kwon, J. You, C. Jia and J. Kim, Facile preparation of nanocellulose/Zn-MOF-based catalytic filter for water purification by oxidation process, *Environ. Res.*, 2022, **205**, 112417.